Supporting Information

Shuman et al. 10.1073/pnas.1321022111

SI Materials and Methods

Reagents and Buffers. All experiments were performed in KMg25 buffer [60 mM 3-(N-morpholino)propanesulfonic acid (MOPS), 25 mM KCl, 1 mM MgCl$_2$, 1 mM EGTA, and 1 mM DTT] in the presence of 20 μM free calmodulin. Apyrase VII, pyruvate kinase, and phospho(enol)pyruvate were obtained from Sigma.

Protein Preparation. Myosin-Ib (Myo1b) containing the motor domain and the first isoleucine-glutamine (IQ) motif of the lever arm helix with calmodulin bound in the nucleotide-free state (Myo1b^{IQ}), containing a C-terminal AviTag and FLAG tag, was expressed and purified as previously described (1). Myo1b^b consisted of the motor domain, complete regulatory domain with five IQ motifs, a C-terminal FLAG tag for affinity purification, and a C-terminal AviTag for site-specific biotinylation. This construct was expressed and purified as described by Lin et al. (2). The Myo1b^{ΔN} protein construct was generated by removing residues 1–13 from the Myo1b^b construct. The native M14 residue was used as the start methionine. Actin was purified from rabbit skeletal muscle (3), and calmodulin were prepared as described previously (4). TRITC-phalloidin–decorated actin, pyrene-labeled actin, and N-ethyl maleimide–modified myosin from rabbit skeletal muscle were prepared as described previously (5).

Crystallization of Myo1b^{IQ}. Crystals of Myo1b^{IQ} (10 mg·mL^{-1}) in 10 mM MOPS (pH 7.2), 50 mM KCl, 1 mM DTT, and 1 mM EGTA were obtained at 4 °C by vapor diffusion in hanging drops by mixing 2.0 μL of protein solution and 2.0 μL of well solution [100 mM Hepes (pH 7.0), 100 mM Li Acetate, and 10% PEG 3350]. Crystals belonging to the monoclinic P2$_1$ space group grew as clustered plates. For data collection, crystals were flash-frozen in liquid nitrogen from a cryosolution consisting of crystallization buffer supplemented with 11% PEG 1,000 and 11% PEG 400.

Crystallographic Structure Determination of Myo1b^{IQ}. X-ray data collection was carried out at National Synchrotron Light Source beamline X6A. Data were indexed and scaled using HKL-2000 (HKL Research, Inc.) (6). The molecular replacement solution was found using Phaser-MR in the program Phenix (7) with the motor domain of nucleotide-free Myo5 (Protein Data Bank ID code 1OE9) as the search model. The convertor domain and then the calmodulin-IQ domain, both from PDB ID code 1OE9, were then sequentially added manually with the Crystallographic Object-Oriented Toolkit (Coot) program (8), with rigid-body refinements performed using the Phenix program as intermediate steps. The resultant model was rebuilt using the AutoBuild component of Phenix and manually completed using the Coot program. Final refinements were carried out alternately with Phenix. The statistics of the final Phenix-refined model are given in Table S1. Structural alignments in the figures were performed using PyMOL.

Cryo-EM Sample Preparation. Actin for cryo-EM samples was polymerized to a final concentration of 51.6 μM in KMg50 buffer [10 mM MOPS (pH 7.0), 1 mM EGTA, 1 mM DTT, 1 mM MgCl$_2$, and 50 mM KCl] with phalloidin added at equimolar levels with the actin. Myo1b in KMg50 was added at ~1.5 molar excess to the actin and spun for 10 min in an ultracentrifuge at 365,000 × g in a TLA-120.2 rotor (Beckman Coulter). The pellet was resuspended in KMg10 [10 mM MOPS (pH 7.0), 1 mM EGTA, 1 mM DTT, 1 mM MgCl$_2$, and 10 mM KCl] to achieve a final concentration of ~20 μM actomyosin. Cryogrids were prepared by diluting ~1.1 μL of the actomyosin mixture ~2.5-fold in distilled water. To minimize complex dissociation during sample preparation (9), the preceding mixture was applied to a non–glow-discharged holey carbon grid (Quantifoil). After ~2 min, the grid was blotted to near dryness with the edge of a piece of filter paper and then rapidly blotted on the front side and plunge-frozen in a manual cryopreparation apparatus.

Cryo-EM Data Collection and Image Processing. Images (~150) were collected at a magnification of ~120,000× on an FEI F20 field emission gun-equipped cryoelectron microscope, using a Gatan US4000 CCD detector, for a final pixel size of ~1.37 Å. Defocus and astigmatism of the micrographs were quantified using CTFFIND3 (10). Actomyosin filaments were boxed manually from phase-corrected micrographs (approximately one box per 27.6-Å repeat) to generate a stack of ~90,000 filament segments. The first and second 45,000 of these segments were analyzed separately using the Iterative Helical Real Space Reconstruction (IHRSR) algorithm (11) as implemented in the single particle analysis for resolution extension (SPARX) package (12), yielding a "gold-standard" resolution estimate of ~26 Å (FSC = 0.5; Fig. S5). The starting model for the IHRSR step was obtained using atomic coordinates from a previous study (13) of the actomyosin complex, filtered to a resolution of ~50 Å to avoid reference bias. Converged helical parameters from the refinement were 27.4 ± 0.2 Å rise per subunit and 167.0° of twist per subunit. For depiction and crystal structure fitting, the reconstructed volume was filtered to the indicated resolution of 26 Å. The crystal structure of nucleotide-free Myo1b was fitted into the EM density map as a rigid body by filtering a synthetic map generated from the X-ray coordinates to a resolution of 26 Å; a translation and rotation search was then performed to maximize the intermap correlation coefficient using the "Fit in Map" function of the UCSF Chimera (14).

Stopped-Flow Transient Kinetics. Transient kinetic fluorescence measurements using pyrene-labeled actin were performed as described previously (15). The temperature was maintained at 20 °C by a circulating water bath. All experiments were performed using 0.5 μM actin and myosin and 20 μM free calmodulin after mixing unless otherwise noted. ADP and ATP concentrations were determined before each transient kinetic experiment by absorbance. For all experiments measuring ATP binding to apo-myosin, actomyosin was pretreated for 10 min with 0.02 U/mL apyrase to remove any residual ADP contamination. In addition, the tight ADP affinity of Myo1b^{ΔN} necessitated that we include 100 U/mL pyruvate kinase and 0.5 mM phospho(enol)pyruvate in the buffer containing the ATP to remove any ADP impurities found in the ATP. The rate of ADP release was measured by incubating 0.5 μM pyrene-actomyo1b with 10 μM ADP and then adding a saturating concentration of ATP (4 mM; all concentrations are final concentrations after mixing). The resulting fluorescence transient had only a single phase with a rate equal to the rate of ADP release (k_{+5}'). The fluorescence transients were initially collected at a higher sampling rate at short time scales to look for a potential fast phase. They were resampled at a slower rate for the sake of presentation.

Optical Trapping Chamber Preparation. Optical trapping chambers were prepared as described previously (5), with the following modifications. Solutions were added sequentially to the chamber as follows: 0.1 mg/mL streptavidin in water (5 min); 1 mg/mL BSA in KMg25 (2× wash for 5 min each wash); 2–10 nM biotinylated

Myo1b in KMg25 + 20 μM calmodulin (5 min); 2× wash with KMg25 buffer; and 1 nM TRITC phalloidin-labeled F-actin in KMg25 with 1 mg/mL glucose, 1 mg/mL BSA, the desired concentration of ATP, 20 μM calmodulin, 100 U/mL pyruvate kinase, 0.5 mM phosphor(enol)pyruvate, 192 U/mL glucose oxidase, and 48 μg/mL catalase (Roche). Beads coated with N-ethyl maleimide–modified myosin were then added to one side of the chamber to replace ~1/4 of the volume of the chamber.

Optical Trapping. Single-molecule actomyosin interactions were recorded using the three-bead assay geometry in a dual-beam optical trap system as previously described (5, 16). The stage position was stabilized using a separate position detection laser that was projected onto the surface-bound bead. The position of the bead was monitored using a quadrant photodiode, and the output of this signal was fed through an analog feedback loop to prevent stage drift as done previously (1). The force dependence of actomyo1b$^{\Delta N}$ detachment was measured by monitoring the force and the attachment durations of individual actomyosin-binding events, driven by Brownian motion.

Measurements of Reversals of the Power Stroke Under Force. An isometric optical clamp was used to apply a dynamic load to the actomyosin to keep the actin filament near its isometric position during the myosin working stroke as described (5, 17, 18). The response time of the feedback loop in the absence of interactions was adjusted to 50 ms. A positive force is defined as a force that opposes the myosin working stroke.

Event Selection and Ensemble Averaging. To determine the start and end points of actomyosin attachments, a covariance threshold selection was used as described (5). Ensemble averages were constructed by synchronizing single-molecule interactions and then averaging the interactions forward and reverse in time as described (5, 19, 20).

Analysis of Power Stroke Reversals. Actomyosin-binding events were selected using the covariance threshold as described above utilizing custom software written in MATLAB (MathWorks). For each binding event, the data were smoothed over a 50-ms running window and the derivative was calculated. The derivative was then smoothed using a Savitzky–Golay filter. Reversals were selected by requiring that the derivative exceed both a positive threshold and a negative threshold for at least 25 ms. This requirement ensured that baseline drift would not cause false identification of reversals.

Error Analysis and Statistics. All errors calculated from fitted parameters were determined from the errors in the fits. All errors in parameters derived from fitted parameters were calculated by propagating the uncertainties. When appropriate, significance was tested using a two-tailed Student t test. When dealing with multiple comparisons, the Bonferroni correction was used to evaluate significance. For the analysis of the force dependence of actomyosin detachment, the data points are not normally distributed; thus, uncertainties were calculated using maximum likelihood estimation and bootstrapping simulations of the data as described previously (5). Uncertainties in fraction of the time spent reversed were derived from 1,000 bootstrapping simulations of the data.

1. Laakso JM, Lewis JH, Shuman H, Ostap EM (2010) Control of myosin-I force sensing by alternative splicing. *Proc Natl Acad Sci USA* 107(2):698–702.
2. Lin T, Tang N, Ostap EM (2005) Biochemical and motile properties of Myo1b splice isoforms. *J Biol Chem* 280(50):41562–41567.
3. Spudich JA, Watt S (1971) The regulation of rabbit skeletal muscle contraction. I. Biochemical studies of the interaction of the tropomyosin-troponin complex with actin and the proteolytic fragments of myosin. *J Biol Chem* 246(15):4866–4871.
4. Putkey JA, Slaughter GR, Means AR (1985) Bacterial expression and characterization of proteins derived from the chicken calmodulin cDNA and a calmodulin processed gene. *J Biol Chem* 260(8):4704–4712.
5. Laakso JM, Lewis JH, Shuman H, Ostap EM (2008) Myosin I can act as a molecular force sensor. *Science* 321(5885):133–136.
6. Otwinowski Z, Minor W (1997) Processing of X-ray diffraction data collected in oscillation mode. *Methods Enzymol* 276:307–326.
7. Adams PD, et al. (2010) PHENIX: A comprehensive Python-based system for macromolecular structure solution. *Acta Crystallogr D Biol Crystallogr* 66(Pt 2): 213–221.
8. Emsley P, Lohkamp B, Scott WG, Cowtan K (2010) Features and development of Coot. *Acta Crystallogr D Biol Crystallogr* 66(Pt 4):486–501.
9. Sindelar CV, Downing KH (2007) The beginning of kinesin's force-generating cycle visualized at 9-A resolution. *J Cell Biol* 177(3):377–385.
10. Mindell JA, Grigorieff N (2003) Accurate determination of local defocus and specimen tilt in electron microscopy. *J Struct Biol* 142(3):334–347.
11. Egelman EH (2010) Reconstruction of helical filaments and tubes. *Methods Enzymol* 482:167–183.
12. Behrmann E, et al. (2012) Real-space processing of helical filaments in SPARX. *J Struct Biol* 177(2):302–313.
13. Holmes KC, Angert I, Kull FJ, Jahn W, Schröder RR (2003) Electron cryo-microscopy shows how strong binding of myosin to actin releases nucleotide. *Nature* 425(6956):423–427.
14. Pettersen EF, et al. (2004) UCSF Chimera—A visualization system for exploratory research and analysis. *J Comput Chem* 25(13):1605–1612.
15. Lewis JH, Lin T, Hokanson DE, Ostap EM (2006) Temperature dependence of nucleotide association and kinetic characterization of myo1b. *Biochemistry* 45(38): 11589–11597.
16. Finer JT, Simmons RM, Spudich JA (1994) Single myosin molecule mechanics: Piconewton forces and nanometre steps. *Nature* 368(6467):113–119.
17. Takagi Y, Homsher EE, Goldman YE, Shuman H (2006) Force generation in single conventional actomyosin complexes under high dynamic load. *Biophys J* 90(4): 1295–1307.
18. Takagi Y, Shuman H, Goldman YE (2004) Coupling between phosphate release and force generation in muscle actomyosin. *Philos Trans R Soc Lond B Biol Sci* 359(1452): 1913–1920.
19. Veigel C, et al. (1999) The motor protein myosin-I produces its working stroke in two steps. *Nature* 398(6727):530–533.
20. Chen C, et al. (2012) Kinetic schemes for post-synchronized single molecule dynamics. *Biophys J* 102(6):L23–L25.
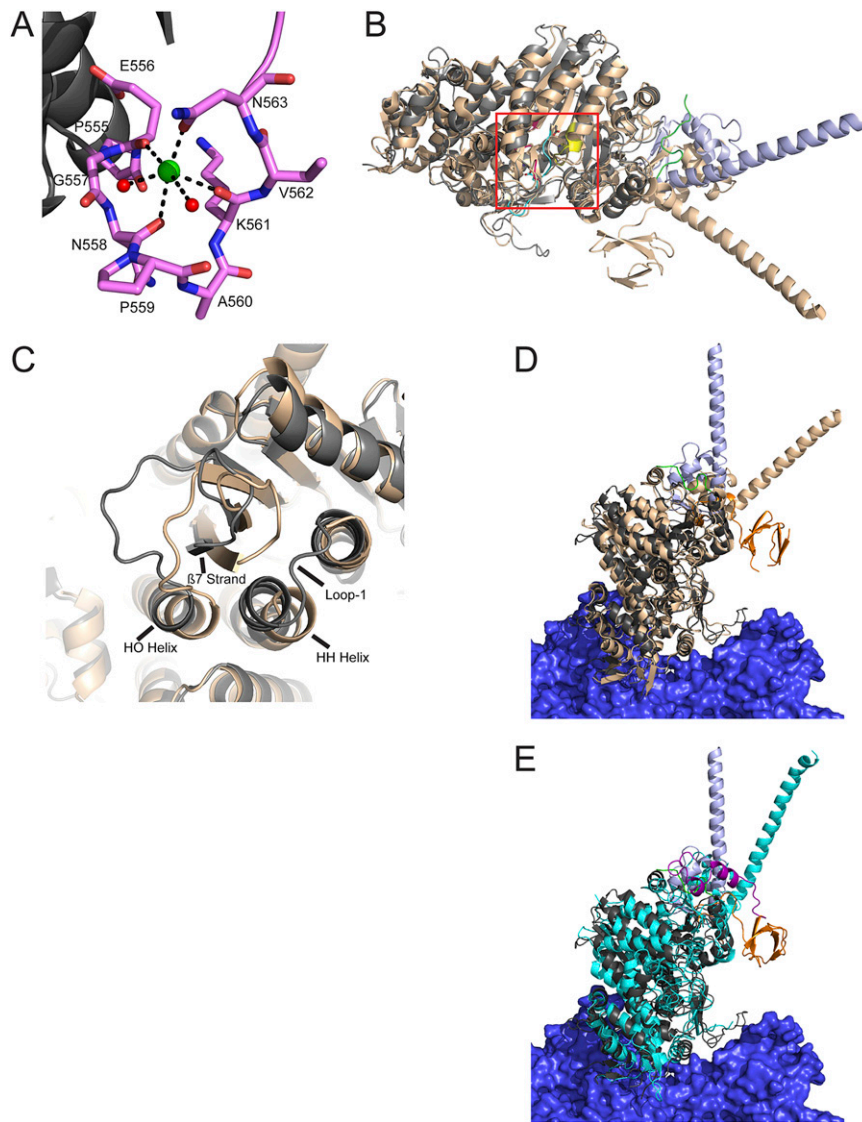
Fig. S1. (*A*) Myo1b[IQ] actin-binding loop (loop-2) is stabilized by a bound cation. (*B*) Overlay of Myo1b[IQ] (gray and light blue) and Myo5 [Protein Data Bank (PDB) ID code 1OE9] (tan), based on structural alignment of the motor domains (residues 26–607 of Myo1b[IQ] and residues 80–673 of Myo5). (*C*) Overlay of the motor domains of Myo1b[IQ] (gray) and Myo5 (tan) shows that there is an additional twisting of the Myo1b[IQ] β-sheet strand-6 and strand-7 in the central β-sheet, which is accompanied by movements of the HO and HH helices. Overlay of Myo1b[IQ] and Myo5 (*D*) and overlay of Myo1b[IQ] and Myo2 (PDB ID code 2MYS) (cyan) (*E*) docked onto actin show the different positions of the lever arm helix. Docking to the actin filament was accomplished by aligning the lower 50-kDa regions of Myo1b[IQ], Myo5, and Myo2 to the 8-Å cryo-EM structure of actin-bound *Dictyostelium* myosin-IE (PDB ID code 4A7F). The light chains were removed for clarity.

Fig. S2. Myo1b^IQ N-terminal region (NTR) makes hydrophobic contacts with the motor and converter domains. (*A*) Surface representation of the Myo1b core motor domain, converter domain, and calmodulin, with the hydrophobic pocket (residues V17, V21, L22, L23, Y47, S50, F77, Y78, P82, F634, and F694) shown in yellow. The NTR is shown in green and yellow as sticks. NTR residues L10, L11, M14, and I15 make hydrophobic interactions in the pocket. The large image corresponds to the boxed region in *Inset*. (*B*) Complementary representation of the NTR as a surface with hydrophobic residues colored yellow. The residues comprising the hydrophobic pocket are shown as sticks.
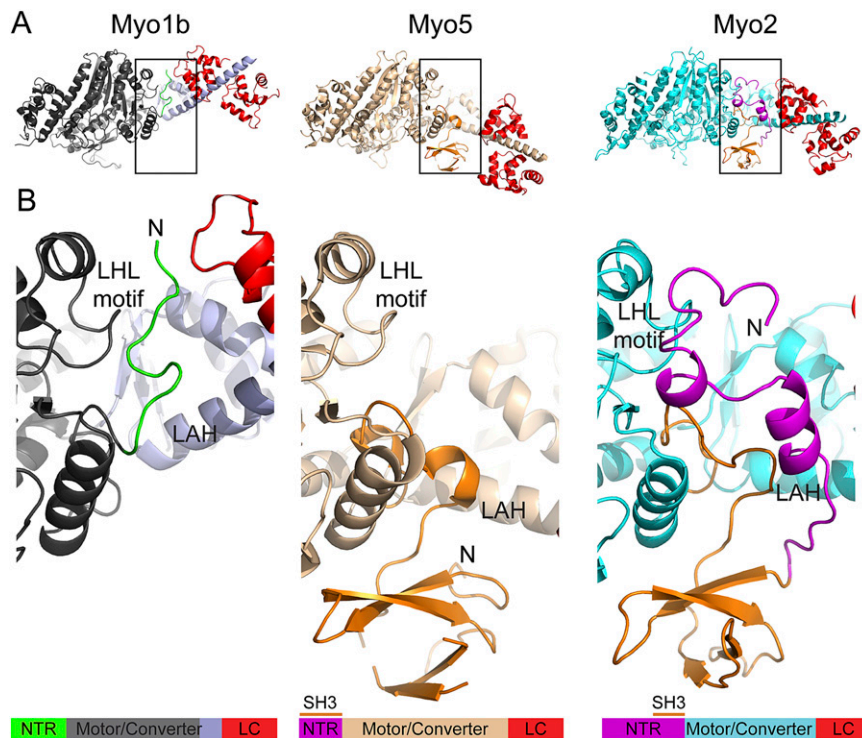
Fig. S3. Comparison of the NTRs of Myo1b[IQ], Myo5, and Myo2. (*A*) Cartoon representation of Myo1b, Myo5, and Myo2. The NTR of Myo1b is colored green, whereas that of Myo2 is colored purple. The SH3-like domains of Myo5 and Myo2 (orange) are distinct from the NTR. (*B*) Enlargement of the boxed area in *A* shows the location of the NTRs. LAH, lever arm helix; LC, light chain; LHL, loop–helix–loop; N, N terminus.
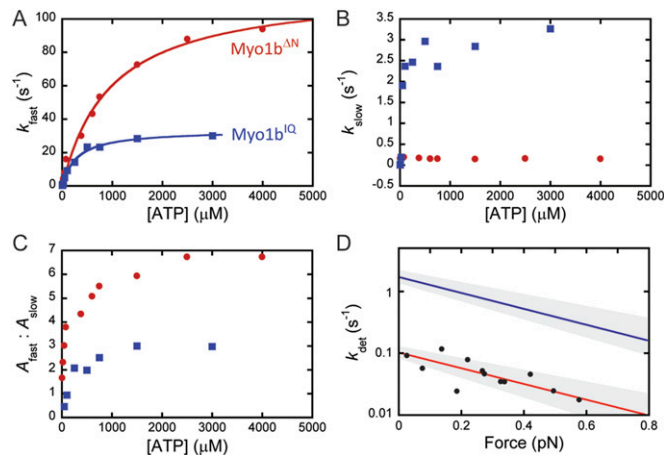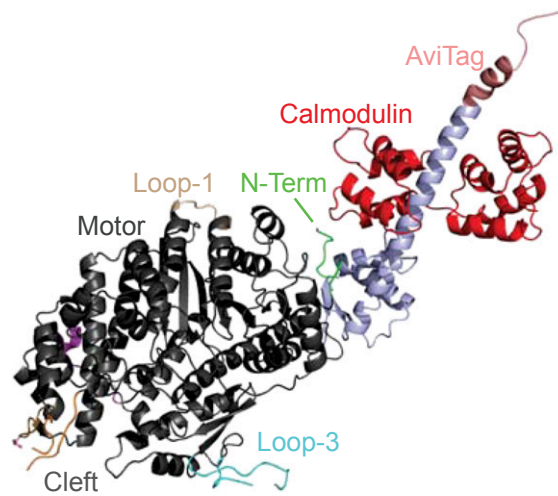

Fig. S4. Stopped-flow transient kinetic measurements of the rates of ATP-induced actomyosin dissociation (*A–C*) and measurement of the force-sensitive detachment kinetics for Myo1b[ΔN] (red) and Myo1b[IQ] (blue) (*D*). All data were interpreted according to Scheme 1, and a summary of the data can be found in Table 1. (*A*) Rate of ATP-induced actomyosin dissociation was measured by rapidly mixing 0.5 μM pyrene-actomyo1b (after mixing) with varying concentrations of ATP and monitoring the increase in pyrene fluorescence as the actin and myosin dissociate. The resulting transients were composed of two phases. The rate of the fast phase is plotted as a function of ATP concentration, and a hyperbolic function was fit to the data. The maximal rate of ATP binding (k_{+2}') and the equilibrium constant for the formation of the ATP collision complex ($1/K_1'$) are derived from the hyperbolic fit. (*B*) Slow phase of the fluorescence transient for ATP-induced actomyosin dissociation was plotted as a function of the ATP concentration. The maximal rate (i.e., [ATP] > 500 μM) reports the rate of the nucleotide-free isomerization from a state that is incapable of binding ATP to a state that is capable of binding ATP ($k_{+\alpha}$). (*C*) Ratio of the amplitude (A) of the fast and slow phases of ATP-induced actomyosin dissociation at saturating ATP concentrations (i.e., [ATP] > 500 μM) reports the equilibrium constant for the nucleotide-free isomerization (K_α). (*D*) Force sensitivity of Myo1b[ΔN] (black circles) was measured as described in *SI Materials and Methods*. The calculated values based on the data can be found in Table 2. The attachment duration as a function of force was measured, and the data were fit to Eq. **1** using maximum likelihood estimation, allowing us to determine the values of the rate of the primary force-dependent transition (k_0) and the distance to the transition state (*d*). The data were ordered by force and averaged over every 20 data points. The detachment rate (k_{det}) was calculated by taking the inverse of the average attachment duration. Each point is the average of 20 points. The gray-shaded area between the red lines shows the 95% confidence interval as determined by bootstrapping and maximum likelihood estimation of the unaveraged data. The red line is the best fit of the model, and the shaded area shows the 95% confidence interval. The blue line shows the best-fit parameters for Myo1b[b], and the shaded area around this line shows the 95% confidence interval as determined previously (5).

Fig. S5. Resolution of the rigor Myo1b–actin complex by fourier shell correlation (FSC) analysis, indicating a nominal resolution of ~27 Å. To minimize the effects of solvent region background noise on the resolution estimate, soft-edged masks (cosine-edge; 50-Å fall-off radius) were derived from the half-dataset volumes (each volume was refined independent of the other; *SI Materials and Methods*) and applied before computing the FSC.

Table S1. Data collection and refinement statistics

Data collection	
Wavelength, Å	1.0000
Space group	P2$_1$*
Cell dimensions	
a, b, c; Å	114.19, 45.09, 115.54
α, β, γ; °	90, 117.18, 90
Resolution, Å	2.22–40.0 (2.29–2.22)[†]
R_{merge}, %	11.5 (45.7)[‡]
I/σI	20.9 (3.9)
Completeness, %	100.0 (87.8)
Redundancy	7.5 (7.0)
Refinement	
Resolution, Å	2.3–40.0 (2.3–2.4)
No. of reflections	52,157
R_{work}/R_{free}	19.0/25.0[§,¶]
No. of atoms	
Protein	7,145
Water	442
Ligand	15
B-factor atoms	
Protein, Å^2	44.4
Water, Å^2	39.4
Ligand, Å^2	48.5
r.m.s.d. bond	
Lengths, Å	0.01
Angles, °	1.2
Ramachandran	
Favored, %	97
Outliers, %	0

*Data from a single crystal.
[†]Values in parentheses are for the highest resolution shell.
[‡]$R_{merge} = \sum |(I - \langle I \rangle)|I\sigma(I)$, where I is the observed intensity.
[§]$R_{work} = \sum_{hkl}||F_o| - |F_c||/\sum_{hkl}|F_o|$, calculated from working dataset, where F_o and F_c are observed and calculated structure factors, respectively.
[¶]R_{free} is calculated from 5% of the data randomly chosen and excluded from refinement.

Movie S1. Structure of Myo1b^{IQ}. The movie shows key structural elements observed in Myo1b^{IQ}, including loop-2, which is stabilized by a coordinated ion. The nucleotide-binding site is compared with that of Myo5, showing an additional turn of its helix. The novel lever arm helix (LAH) position of Myo1b^{IQ}, compared with those of apo-Myo5 and near-rigor Myo2, is also highlighted, showing the interactions made by the two sequence insertions. A model of Myo1b^{IQ} docked to actin (PDB ID code 3MFP) is shown, based on EM data. The hydrophobic cavity, formed by the novel LAH position in which the N-terminal region (NTR) resides is shown, as are the interactions between the NTR and motor/LAH regions.

[Movie S1](#)